HHS Public Access

Author manuscript

Anal Chem. Author manuscript; available in PMC 2024 August 18.

Published in final edited form as:

Anal Chem. 2023 March 28; 95(12): 5214–5222. doi:10.1021/acs.analchem.2c04795.

Nano-DESI Mass Spectrometry Imaging of Proteoforms in Biological Tissues with High Spatial Resolution

Manxi Yang[1], **Daisy Unsihuay**[1,†], **Hang Hu**[1], **Frederick Nguele Meke**[2], **Zihan Qu**[1,2], **Zhong-Yin Zhang**[1,2], **Julia Laskin**[*,1]

[1] Department of Chemistry, Purdue University, West Lafayette, IN, 47907, USA

[2] Department of Medicinal Chemistry and Molecular Pharmacology, Purdue University, West Lafayette, IN, 47907, USA

Abstract

Mass spectrometry imaging (MSI) is a powerful tool for label-free mapping of the spatial distribution of proteins in biological tissues. We have previously demonstrated imaging of individual proteoforms in biological tissues using nanospray desorption electrospray ionization (nano-DESI), an ambient liquid extraction-based MSI technique. Nano-DESI MSI generates multiply charged protein ions, which is advantageous for their identification using top-down proteomics analysis. In this study, we demonstrate proteoform mapping in biological tissues with a spatial resolution down to 7 μm using nano-DESI MSI. A substantial decrease in protein signals observed in high spatial resolution MSI makes these experiments challenging. We have substantially enhanced the sensitivity of nano-DESI MSI experiments by optimizing the design of the capillary-based probe and the thickness of the tissue section. In addition, we demonstrate that oversampling may be used to further improve spatial resolution at little or no expense to sensitivity. These developments represent a new step in MSI-based spatial proteomics, which complements targeted imaging modalities widely used for studying biological systems

Graphical Abstract

[*] **Corresponding Author Julia Laskin** – Department of Chemistry, Purdue University, West Lafayette, IN, 47907, United States; jlaskin@purdue.edu.

[†] Present Addresses: Daisy Unsihuay – Department of Pathology and Laboratory Medicine, University of Pennsylvania, Philadelphia, PA, 19104, USA

Author Contributions

All authors have given approval to the final version of the manuscript.

ETHICS STATEMENT

The animal studies were reviewed and approved by the Institutional Animal Care and Use Committees (IACUC) of Purdue University.

ASSOCIATED CONTENT

Supporting Information

The Supporting Information is available free of charge on the ACS Publications website.

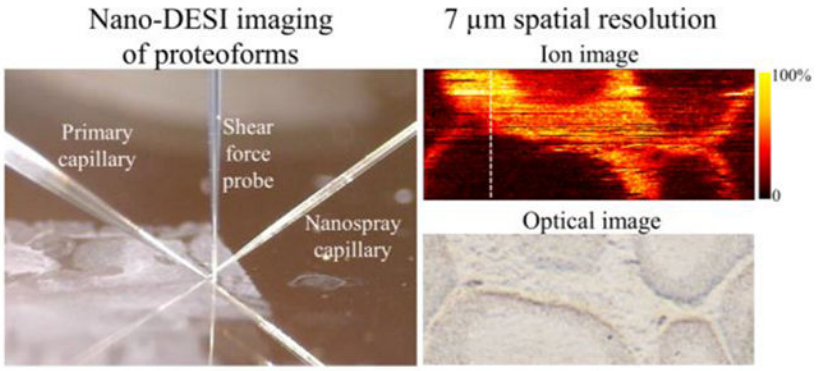

INTRODUCTION

Protein imaging plays an important role in studying biological systems. Antibody-based optical methods including brightfield immunohistochemistry (IHC)[1] and immunofluorescence (IF)[2,3] are the most widely used techniques for visualizing protein localization in cells and tissues using fluorescent labeling. High spatial resolution and speed of analysis are their key advantages.[4–7] Meanwhile, limited multiplexing capabilities of these techniques have been a major driving force for the development of new approaches for spatial proteomics. CO-Detection by indEXing (CODEX) employs DNA-conjugated fluorescently-labeled antibodies to target proteins of interest.[8] Up to 60 target proteins can be visualized in the same sample using the sequential addition and removal of fluorophore-labeled DNA barcodes.[8–11]

Targeted proteomics approaches based on immunolabeling have been also coupled with mass spectrometry (MS) analysis, which substantially enhances the multiplexing capabilities at the expense of the spatial resolution. For example, imaging mass cytometry uses antibodies tagged with rare earth metals as mass reporters. Imaging of metal tags is performed using inductively coupled plasma time-of-flight (ICP-TOF) MS. This approach has been used for simultaneous imaging of up to 40 proteins with a subcellular spatial resolution.[12–16] Multiplexed ion-beam imaging (MIBI) is another highly multiplexed targeted imaging method in which spatial profiling of metal labels is performed using secondary ion mass spectrometry. MIBI has been typically used to image ~35–45 protein targets with the potential to target up to 100 proteins with a spatial resolution down to 250 nm.[17–21] Recently, a multiplexed immunohistochemical MALDI-MS imaging (MALDI-IHC) with photocleavable mass tags has been developed and used for targeted imaging of up to 12 proteins with 10 µm spatial resolution.[22] Despite the power of targeted spatial proteomics methods, they are limited by the costly and laborious process of the development and validation of affinity reagents.[23] Furthermore, antibody-based imaging techniques have limited capabilities for targeting post-translational modifications (PTM).[24,25] Label-free approaches have attracted considerable attention in studies focused on the untargeted protein imaging including the discovery of disease biomarkers and understanding of complex biochemical pathways associated with health and disease.[26–29] Raman spectroscopy imaging is a well-established noninvasive label-free imaging modality, which has been widely used for imaging of living cells with subcellular spatial resolution.[30,31] Although Raman spectra

of individual proteins contain characteristic features in the fingerprint region[32], substantial spectral overlap presents a challenge to the identification of protein signals observed in imaging experiments.[30,31,33]

Mass spectrometry imaging (MSI) is ideally suited for the label-free imaging of proteins in biological samples with unprecedented chemical specificity.[34] MSI techniques are intrinsically multiplexed providing spatial localization of many proteins in one experiment with a spatial resolution of ~50–100 μm.[35,36] Matrix-assisted laser desorption ionization (MALDI) is typically used for imaging of intact proteins[37–42]. In these experiments, bottom-up or off-line top-down proteomics approaches have been used for protein identification.[43–47] Meanwhile, nanodroplet processing in one pot for trace samples (nanoPOTS)[48] has been developed to enable simultaneous imaging and identification of proteins with a spatial resolution of 50–100 μm, using bottom-up proteomics coupled with laser capture microdissection.[49]

Top-down proteomics is a powerful tool for protein identification based on the accurate mass measurement and fragmentation patterns of intact proteins obtained using MS/MS.[50] MS analysis of intact proteins preserves post-translational modifications (PTM) and there by enables the identification of individual proteoforms, which provide insights into the state of cells of the same type in different parts of the biological system.[51–54] Recent developments in MSI techniques that utilize ambient ionization based on liquid extraction have enabled imaging of intact proteins in biological samples. These techniques generate higher charge states of protein ions, which is particularly advantageous for their identification using on-tissue top-down proteomics. Desorption electrospray ionization (DESI) and liquid extraction surface analysis (LESA) have been used for detecting intact proteins in tissues[55] with a spatial resolution of 150–200 μm[56,57] and 1 mm,[58,59] respectively. Nanospray desorption electrospray ionization (nano-DESI) is a liquid extraction-based ambient ionization technique that has been used for imaging of intact proteins and protein complexes in tissues with high sensitivity.[60–65] Protein identification is performed using on-tissue MS/MS combined with database searching.[60] Although the spatial resolution of 43 μm has been achieved in one study[62], most nano-DESI MSI of proteins has been performed with a spatial resolution of 80–200 μm.[60,61,63,64] Meanwhile, a spatial resolution of better than 10 μm has been achieved in nano-DESI MSI of lipids and metabolites by finely pulling the capillaries comprising the nano-DESI probe and introducing a shear force probe that enables constant distance mode scanning.[66–68] Herein, we adapt this approach to imaging of proteoforms in tissues. Using mouse brain tissue as a model system, we demonstrate mapping of proteoforms with a spatial resolution down to 7 μm.

MATERIALS AND METHODS

Chemicals and Materials.

HPLC grade water was obtained from MilliporeSigma (Burlington, MA). HPLC grade acetonitrile (ACN) was obtained from Fisher chemical (Hampton, NH). Ethanol 200 proof was purchased from Decon Laboratories, INC (King of Prussia, PA). 99.8+% chloroform was purchased from Alfa Aesar (Tewksbury, MA). Optima™ LC/MS Grade formic acid (FA) was purchased from Fisher Scientific (Hampton, NH). 99^{+}% 19:0

lysophosphatidylcholine, LPC(19:0), was purchased from Avanti Polar Lipids (Birmingham, AL) and used for optimization of the nano-DESI probe. Polymicro Flexible Fused Silica Capillary Tubing (OD 150μm, ID 50 μm; OD 360μm, ID 100 μm; and OD 800μm, ID 200μm) were from Molex (Thief River Falls, MN). PathScan Enabler IV (Meyer Instruments, Inc) was used to acquire the optical images of the tissue sections before and after washing.

Animal Tissues.

Brain tissues of C57BL/6 mice were used in this study under the approval of IRB. Adult (3–6-month-old) mice were euthanized by CO_2 inhalation followed by cervical dislocation, after which their brains were collected, snap frozen in isopentane kept over dry ice, and stored at −80 °C.[69,70] Tissues were sectioned sagittally at −21 °C using a CM1850 Cryostat (Leica Microsystems, Wetzlar, Germany). Two adjacent 12 μm-thick and 25 μm-thick sections were thaw mounted side-by-side onto each glass microscope slide (IMEB, Inc Tek-Select Gold Series Microscope Slides, Clear Glass, Positive Charged). The sections were stored in a −80 °C freezer. For nano-DESI MSI analysis, tissue sections were allowed to thaw at room temperature and then immersed into serial ethanol solutions (70%, 90% and 100%) for 20 s each to precipitate proteins. Lipids were washed off by immersing the sample into 99.8% chloroform for 25 s right before nano-DESI MSI analysis.[56,71]

Nano-DESI MSI.

Imaging experiments were performed on an Agilent 6560 ion mobility (IM) quadrupole time-of-flight (Q-TOF) instrument equipped with a custom-designed nano-DESI source. Details of the nano-DESI source can be found in our previous publication.[66,67] Briefly, the nano-DESI probe was assembled using two fused silica capillaries with the tip pulled to ~10 μm in diameter, positioned at a ~90–120-degree angle. In this study, we flame-pulled both sides of the nanospray capillary to ~10 μm. Pulling the side of the capillary that faces the mass spectrometer makes it easier to achieve a stable signal of proteins. ACN/H_2O/FA (80/20/0.1, v/v/v) containing 100 nM LPC(19:0) internal standard (IS) was used as extraction solvent. The solvent flow rate was kept at 0.2 μL/min. Tissue samples were placed on a motorized XYZ stage controlled by a custom-designed LabVIEW program.[66] Nano-DESI MSI experiments were performed by scanning the sample under the nano-DESI probe at a scan rate of 12 μm/s. The step between the lines was set to 15 μm and 7 μm in the experiments performed without and with oversampling, respectively.

All imaging experiments were performed in positive ionization QTOF-only mode with the standard mass range of the high mass resolution and extended dynamic range mode. The instrument was calibrated using Agilent ESI-L Low concentration tuning mix/0.1 mM HP-0321/ACN/H_2O (10 mL/3 μL/85.5 mL/4.5 mL). The gas temperature was set to 300 °C. The capillary voltage was 4000 V. The Quad AMU was set to 200 amu to improve transmission of large protein ions. High pressure funnel RF, trap funnel RF and rear funnel RF were set to 180 V, 200 V and 180 V, respectively. The acquisition rate was 1 Hz.

Data Analysis.

Endogenous protein species observed in MSI experiments were identified using on-tissue top-down proteomics analysis described in our previous study.[60] Briefly, targeted MS/MS analysis of proteins of interest was performed on a tissue section adjacent to the imaged section by scanning the nano-DESI probe over the regions of interest where the proteins are localized. Proteins were then identified by matching their intact masses and MS/MS fragmentation patterns against the UniProt database.[72–75]

Ion images were generated from .d files using a previously described workflow.[76] In this workflow, Skyline software is used to extract signal intensities of the most abundant isotopic peaks of each charge state of proteins of interest in each pixel into a .txt file. Ion images are generated from the .txt file using a custom Python script developed by our group (https://github.com/hanghu1024/RAW-MSI-generator). Ion images reported in this study were normalized to the total ion current (TIC). Ion chronograms across selected tissue features were extracted to estimate the spatial resolution.

RESULTS AND DISCUSSION

High-spatial-resolution nano-DESI MSI of proteins

The experimental workflow for protein imaging using nano-DESI MSI is shown in Figure 1. It involves tissue sectioning and washing to precipitate proteins and remove lipids that otherwise suppress protein signals. Protein imaging is performed using a high-resolution nano-DESI MSI probe comprised of two finely pulled capillaries and a shear force probe. Additional photos of the customized ion source and the assembled probes are shown in Figure S1. Unlike nano-DESI MSI of lipids, in which comparable signals are observed using moderate- and high-resolution nano-DESI probe, signals of proteins decrease substantially in high-resolution experiments (Figure S2). The reason for the difference in the effect of the spatial resolution of lipid and protein signals in nano-DESI MSI is not fully understood. It may be attributed either to differences in concentrations of lipids and proteins in tissue sections or to differences in the physical properties of the sections before and after washing for protein imaging. In order to improve the sensitivity and signal stability, we optimized the design of the high-resolution nano-DESI probe described in our previous study[66] by pulling the side of the nanospray capillary facing the MS inlet (Figure S1c). We found that, in this configuration, protein signals are less sensitive to the precise positioning of the nanospray capillary at the MS inlet, which makes it easier to obtain a stable signal of imaging experiments. Because the extent of protein signal suppression in MSI is unknown, we did not attempt the normalization to the signal of the internal standard. Future studies will examine matrix effects in protein imaging in order to establish a robust normalization strategy. TIC-normalized ion images are generated to visualize the spatial distribution of endogenous proteoforms, and the identification is performed using on-tissue MS/MS combined with database searching as described in our previous work.[60]

High-resolution nano-DESI MSI of proteins was performed using the cerebellum region of a mouse brain tissue as a model system. The results obtained by imaging a 25 μm-thick tissue section are shown in Figure 2. Additional ion images of the observed proteoforms are

provided in Figure S4. The effect of the thickness of the tissue section will be discussed later in the text.

An optical image of the analyzed mouse brain tissue section is shown in Figure 2a. Ion images of several abundant proteoforms are shown in Figures 2b–i. The spatial distribution of the N-terminal acetylated 14.1 kDa myelin basic protein (MBP) shown in Figure 2b indicates that this protein is localized to the white matter region of the cerebellum, which is consistent with its role in brain. Specifically, MBP is the major component of myelin sheath expressed by oligodendrocytes which are aligned in rows between the nerve fibers of the white matter.[77,78] Meanwhile as expected, hemoglobin subunit alpha is observed in high abundance in blood vessel regions (Figure 2c). Ion images of other representative proteins including ubiquitin, N-terminal acetylated thymosin β−4, acyl-CoA binding protein, cytochrome c oxidase subunit 6B1, and dynein lightchain 2 (Figure 2d, S4e–i), show a fairly uniform distribution of these species in the tissue with slightly higher signals observed in the cerebellar cortex and somewhat lower signals in the white matter region.

Thicker tissue sections yield better signals of endogenous proteins.

A substantial decrease in protein signals in high-resolution nano-DESI MSI experiments may be attributed to the small amount of material extracted from a smaller area sampled by the high-resolution nano-DESI probe. We hypothesized that higher signals may be obtained by analyzing a thicker tissue section. We note that 10–12 μm-thick tissue sections are typically used in nano-DESI MSI experiments. Meanwhile, protein imaging data shown in Figure 2 were acquired using 25 um-thick sections. To investigate the effect of tissue thickness on signal intensity of endogenous proteins, we acquired line scans from similar locations of the adjacent 12 μm- and 25 μm-thick tissue sections placed on the same glass slide. The results obtained for two representative proteins, MBP and ubiquitin, in two different regions of a mouse brain tissue are shown in Figure 3.

Mass spectra shown in Figures 3a and 3b were averaged over small regions of the white matter and cerebellar cortex, respectively, labeled in the optical images. Larger optical images are provided in Figure S3. Different charge states of MBP (yellow circles in Figure 3a) and ubiquitin (green circles in Figure 3b), the most abundant proteoforms observed in the white matter and cerebellar cortex regions, respectively, are labeled in mass spectra. All charge states of both proteoforms show an increase in signal intensity with increase in the thickness of a tissue section. We used the most abundant isotopic peak of the most abundant charge state of each proteoform to estimate the fold change of the signal intensity by taking the ratio of the intensities observed by analyzing the 25 μm- and 12 μm-thick sections. Signals obtained for the most abundant 23+ charge state of MBP, MBP^{23+}, are compared in Figure 3c and the corresponding signal intensities are indicated in the figure. We observe an estimated 2-fold increase in the signal intensity of MBP^{23+} from 1.3×10^4 for the thinner section to 2.4×10^4 for the thicker section. Similar analysis was performed for the most abundant 11+ charge state of ubiquitin, $ubiquitin^{11+}$, as shown in Figure 3d. For this protein, we observe a 1.5-fold signal increase from 4.4×10^3 to 6.6×10^3 with an increase in tissue thickness from 12 μm to 25 μm. Comparison of signal intensities obtained for 12 μm to 25 μm-thick tissue sections and the fold changes obtained in replicate experiments are shown

in Table S1–S2. The regions from where the average signals were obtained are labeled in the optical images of the tissue sections shown in Figure S3. Although the fold changes may vary depending on the experimental conditions, our results demonstrate that higher signals of endogenous proteoforms are obtained using thicker tissue sections. Subsequently, nano-DESI MSI experiments were performed using 25 μm-thick tissue sections.

Oversampling improves the spatial resolution.

As indicated earlier, nano-DESI MSI experiments are performed by scanning the sample under the probe at a constant rate in lines and using a fixed step between the lines. The spatial resolution in nano-DESI MSI is primarily determined by the size of the liquid bridge. Meanwhile, the scan rate of the sample stage, step size between the lines, and acquisition rate of a mass spectrometer may limit the experimentally observed spatial resolution.[79] The influence of these parameters over the size of the liquid bridge becomes particularly important in high-resolution and high-throughput imaging experiments.[80] In this study, the acquisition rate was 1 Hz with the scan rate of 12 μm/s resulting in the pixel size of 12 μm in the scanning direction. The size of the liquid bridge is ~10 μm. Based on these considerations, we estimate that the sampled area that contributes to the signal in a single pixel (sampled area/pixel) in experiments performed in a regular sampling mode (Figure 2) is ~12 × 10 μm^2. In this mode, we used a 15 μm step between the lines to avoid oversampling. Thus, the pixel size in the ion images is 12 × 15 μm^2. Oversampling is an approach, in which the step between the lines is smaller than the size of the liquid bridge.[79]

Previous work by Lanekoff et al. has demonstrated that oversampling effectively increases the spatial resolution of nano-DESI MSI of lipids without causing a redistribution of the lipid analytes.[79] In particular, in that study, oversampling was used to enhance the spatial resolution by reducing the pixel size from 200 μm × 20 μm to 50 μm × 20 μm. The increase in the spatial resolution was attributed to a substantial decrease in the amount of extractable material after the first sampling, which ensures that the contribution of the previously sampled area on the tissue to the signal observed in the next line is quite small. Repeated line scans acquired over the same area have demonstrated a ~25–50% depletion of lipid signals after the first sampling.[79]

We examine the effect of oversampling on the spatial resolution of protein imaging by decreasing the step between the lines from 15 μm to 7 μm. Ion images obtained for a 25 μm-thick tissue section in the oversampling mode are shown in Figure 4. Additional ion images of the observed proteoforms are provided in Figure S5. Figure 4a shows an optical image of the analyzed brain tissue section. Figures 4b–d show the TIC-normalized ion images of the same proteoforms as those shown in Figure 2.

Next, we compare the spatial resolution obtained with and without oversampling. We note that the spatial resolution of MSI experiments does not equal the pixel size. Instead, the experimental resolution is a measure of the capacity of the imaging technique to resolve adjacent features. In our studies, we estimate the spatial resolution by measuring the distance over which the steepest chemical gradients in the sample are observed. In particular, we use extracted ion chronograms (EIC) for a selected *m/z* to measure the distance over which the signal intensity increases from 20% to 80% of its maximum value.[81,82] The results of

this analysis are summarized in Figure 5. We used EIC of MBP^{23+} that show a substantial variation in the signal across the tissue to compare the spatial resolution obtained without (Figure 5a) and with (Figure 5b) oversampling. White lines in the insets in Figures 5a and 5b indicate the direction of the extracted line scan shown in the corresponding figures. The sharpest features highlighted with yellow circles in the inset in Figures 5a and 5b were used to estimate the spatial resolution. Additional results demonstrating the robustness of this estimation by analyzing a different region of the tissue are shown in Figure S6. We estimate that, without oversampling, we achieved the spatial resolution down to 15 μm. Meanwhile, the spatial resolution down to 7 μm was achieved with oversampling. Differences in the spatial resolution achieved without and with oversampling are highlighted in Figure 5 by overlaying the optical image and ion image of MBP^{23+} in a small region of interest. Details of this comparison are provided in Figure S7. The signal of MBP is more tightly localized in the white matter region in the ion image acquired with oversampling (Figure 5b, S7b), whereas MBP signal is somewhat spread outside of the white matter region in the ion image acquired without oversampling (Figure 5a, S7a). Although in order to resolve closely separated features that are 7 μm apart, the distance between each pixel must be smaller than 3.5 μm per the Nyquist criterion[83], we still observe the broadening of the step function by examining the edges of features in the spatial distributions. We obtain a much better definition of the sharp features at higher spatial resolution even when the sampling frequency is smaller than described by the Nyquist criterion. We note that because our approach assumes that chemical gradient is a step function, it provides the upper limit of the spatial resolution. The spatial resolution may be further improved by decreasing the scan rate of the sample stage, which will reduce the pixel size in the scanning direction below 12 μm.

To examine if the improvement in the spatial resolution obtained using oversampling is attributed to the significant depletion of protein analytes after the first line scan, we acquired four repeated line scans from the same locations across mouse brain cerebellum regions on both the 12 μm- and 25 μm-thick tissue sections. The depletion curves showing the decrease in the observed signals of $ubiquitin^{11+}$ and MBP^{23+} with the number of repeated analyses are shown in Figures 6a and 6b, respectively. Additional results obtained from one of the replicate experiments are provided in Figures S8–9 and S10–11 for the 12 μm- and 25 μm-thick tissue sections, respectively.

Regardless of the tissue thickness, we observe a substantially higher abundance of endogenous proteins in the first line scan (Figure S8b, S9b, S10b, S11b), in comparison with the following line scans (Figure S8c–e, S9c–e, S10c–e, S11c–e). By examining the averaged mass spectra (Figure S8e, S9e, S10e, S11e), we concluded that almost no proteins were observed in line 4, which contains only background signals. Therefore, when generating the depletion curves, the averaged mass spectra from the fourth line scans were subtracted from each averaged mass spectrum from the same locations in lines 1–3 to remove the background signal contribution to the protein signals. The protein signals were then normalized to the highest signal intensity among the four repeated line scans. The depletion curves shown in Figure 6 indicate that ~77% of $ubiquitin^{11+}$ was depleted after the first line scan across the 25 μm-thick section with ~10–13% depletion in the following line scans. Meanwhile, ~38% of MBP^{23+} is depleted after the first scan across the 25

μm-thick section followed by a ~47% reduction after the second scan and ~15% depletion after the third scan. We observed a faster protein depletion in repeated scans across the 12 μm section (Figure 6). Specifically, ~85% depletion of ubiquitin^{11+} and ~72% depletion of MBP^{23+} was observed after the first line scan. This result provides additional support for the observed improvement of the spatial resolution using oversampling and is consistent with the observation that 25 μm tissue sections yield better protein signals than 12 μm tissue sections due to the higher amount of endogenous proteoforms in the thicker tissue section. Although oversampling should be particularly beneficial for thin tissue sections, for which there is little or no contribution to the measured signal from previously sampled areas, the significantly lower signal of the endogenous proteoforms obtained using thin sections reduces the overall quality and contrast of ion images.

We note that the depletion rate may be dependent on the tissue type and experimental conditions.[79] In our repeated sampling experiments, we observe a 40%−80% depletion of protein signals after the first scan. It follows that protein signals observed in MSI experiments with oversampling are dominated by proteins extracted from the unsampled tissue, which ensures that oversampling efficiently reduces the extraction area and thereby improves the experimental spatial resolution. We also performed an oversampling experiment using a moderate-resolution probe that generates a larger liquid bridge on a surface. We found that oversampling using a larger volume of the liquid bridge results in dilution of the extracted proteins, which decreases the sensitivity. It follows that there is a tradeoff between the size of the liquid bridge and extent of oversampling that generates good protein signals in imaging experiments.

CONCLUSIONS

We demonstrate imaging of proteoforms with a spatial resolution down to 7 μm using nano-DESI MSI of mouse brain tissue as a model system. The optimization of the nano-DESI probe by finely pulling both sides of the nanospray capillary improves both the sensitivity and stability of protein signals. We demonstrate that thicker tissue sections may be used to further improve signal intensities of endogenous proteoforms. Meanwhile, oversampling is a promising strategy for improving the spatial resolution. This improvement is attributed to the significant depletion of protein signals after the first sampling. Our results show that nano-DESI MSI enables label-free imaging of individual proteoforms with cellular resolution. This development will facilitate spatially-resolved cell typing based on the observed proteoforms, which, in combination with imaging of lipids and metabolites,[84,85] will advance our understanding of biochemical pathways in biological systems.

Supplementary Material

Refer to Web version on PubMed Central for supplementary material.

ACKNOWLEDGMENTS

The authors gratefully acknowledge the financial support from the National Institutes of Health (NIH) Common Fund, through the Office of Strategic Coordination/Office of the NIH Director under awards UG3HL145593 and UH3CA255132 (HuBMAP Program, JL), support from the NIH BRAIN Initiative - Cell Census Network

(BICCN) through grant RF1MH128866 (BICCN), support from NIH RO1 CA069202, and Center for Bioanalytical Metrology, an NSF Industry-University Cooperative Research Center (Grant IIP-1916691).

REFERENCES

(1). De Matos LL, Trufelli DC, De Matos MGL, da Silva Pinhal MA Immunohistochemistry as an Important Tool in Biomarkers Detection and Clinical Practice. Biomark Insights 2010, 5, 9–20. [PubMed: 20212918]

(2). Odell ID; Cook D Immunofluorescence Techniques. Journal of Investigative Dermatology 2013, 133, e4.

(3). Im K; Mareninov S; Diaz MFP; Yong WH An Introduction to Performing Immunofluorescence Staining. Methods Mol Biol. 2019, 1897, 299–311. [PubMed: 30539454]

(4). Lichtman JW; Conchello JA Fluorescence Microscopy. Nat Methods 2005, 2, 910–919. [PubMed: 16299476]

(5). Sanderson MJ; Smith I; Parker I; Bootman MD Fluorescence Microscopy. Cold Spring Harbor Protocols 2014, 2014, pdb–top071795.

(6). Chen R; Zhou H; Li A; Cheng X; Liu X; Huang F; Wang Y; Liu Y; Gong H; Liu X; Zeng S Chemical Sectioning for Immunofluorescence Imaging. Anal. Chem 2021, 93, 8698–8703. [PubMed: 34138541]

(7). Bishop DP; Cole N; Zhang T; Doble PA; Hare DJ A Guide to Integrating Immunohistochemistry and Chemical Imaging. Chem. Soc. Rev 2018, 47, 3770–3787. [PubMed: 29542747]

(8). Black S; Phillips D; Hickey JW; Kennedy-Darling J; Venkataraaman VG; Samusik N; Goltsev Y; Schürch CM; Nolan GP CODEX Multiplexed Tissue Imaging with DNA-Conjugated Antibodies. Nat. Protoc 2021, 16, 3802–3835. [PubMed: 34215862]

(9). Goltsev Y; Samusik N; Kennedy-Darling J; Bhate S; Hale M; Vazquez G; Black S; Nolan GP Deep Profiling of Mouse Splenic Architecture with CODEX Multiplexed Imaging. Cell 2018, 174, 968–981. [PubMed: 30078711]

(10). Kennedy-Darling J; Bhate SS; Hickey JW; Black S; Barlow GL; Vazquez G; Venkataraaman VG; Samusik N; Goltsev Y; Schürch CM; Nolan GP Highly Multiplexed Tissue Imaging Using Repeated Oligonucleotide Exchange Reaction. Eur. J. Immunol. 2021, 51, 1262–1277. [PubMed: 33548142]

(11). Neumann EK; Patterson NH; Rivera ES; Allen JL; Brewer M; deCaestecker MP; Caprioli RM; Fogo AB; Spraggins JM Highly Multiplexed Immunofluorescence of the Human Kidney Using Co-Detection by Indexing. Kidney Int 2022, 101, 137–143. [PubMed: 34619231]

(12). Bandura DR; Baranov VI; Ornatsky OI; Antonov A; Kinach R; Lou X; Pavlov S; Vorobiev S; Dick JE; Tanner SD Mass Cytometry: Technique for Real Time Single Cell Multitarget Immunoassay Based on Inductively Coupled Plasma Time-of-Flight Mass Spectrometry. Anal. Chem 2009, 81, 6813–6822. [PubMed: 19601617]

(13). Giesen C; Wang HA; Schapiro D; Zivanovic N; Jacobs A; Hattendorf B; Schüffler PJ; Grolimund D; Buhmann JM; Brandt S; Varga Z; Wild PJ; Günther D; Bodenmiller B Highly Multiplexed Imaging of Tumor Tissues with Subcellular Resolution by Mass Cytometry. Nat. methods 2014, 11, 417–422. [PubMed: 24584193]

(14). Schulz D; Zanotelli VRT; Fischer JR; Schapiro D; Engler S; Lun XK; Jackson HW; Bodenmiller B Simultaneous Multiplexed Imaging of mRNA and Proteins with Subcellular Resolution in Breast Cancer Tissue Samples by Mass Cytometry. Cell Syst 2018, 6, 25–36. [PubMed: 29289569]

(15). Wang YJ; Traum D; Schug J; Gao L; Liu C; Atkinson MA; Powers AC; Feldman MD; Naji A; Chang KM; Kaestner KH Multiplexed in Situ Imaging Mass Cytometry Analysis of the Human Endocrine Pancreas and Immune System in Type 1 Diabetes. Cell Metab 2019, 29, 769–783. [PubMed: 30713110]

(16). Kuett L; Catena R; Özcan A; Plüss A; Schraml P; Moch H; de Souza N; Bodenmiller B Three-Dimensional Imaging Mass Cytometry for Highly Multiplexed Molecular and Cellular Mapping of Tissues and the Tumor Microenvironment. Nat Cancer 2022, 3, 122–133. [PubMed: 35121992]

(17). Angelo M; Bendall SC; Finck R; Hale MB; Hitzman C; Borowsky AD; Levenson RM; Lowe JB; Liu SD; Zhao S; Natkunam Y; Nolan GP Multiplexed Ion Beam Imaging of Human Breast Tumors. Nat Med 2014, 20, 436–442. [PubMed: 24584119]

(18). Keren L; Bosse M; Marquez D; Angoshtari R; Jain S; Varma S; Yang SR; Kurian A; Van Valen D; West R; Bendall SC; Angelo M A Structured Tumor-Immune Microenvironment in Triple Negative Breast Cancer Revealed by Multiplexed Ion Beam Imaging. Cell 2018, 174, 1373–1387. [PubMed: 30193111]

(19). Ptacek J; Locke D; Finck R; Cvijic ME; Li Z; Tarolli JG; Aksoy M; Sigal Y; Zhang Y; Newgren M; Finn J Multiplexed Ion Beam Imaging (MIBI) for Characterization of the Tumor Microenvironment across Tumor Types. Laboratory Investigation 2020, 100, 1111–1123. [PubMed: 32203152]

(20). Liu CC; Mccaffrey EF; Greenwald NF; Soon E; Risom T; Vijayaragavan K; Oliveria JP; Mrdjen D; Bosse M; Tebaykin D; Bendall SC; Angelo M Multiplexed Ion Beam Imaging: Insights into Pathobiology. Annu. Rev. Pathol. 2022, 17, 403–423. [PubMed: 34752710]

(21). Keren L; Bosse M; Thompson S; Risom T; Vijayaragavan K; Mccaffrey E; Marquez D; Angoshtari R; Greenwald NF; Fienberg H; Wang J; Kambham N; Kirkwood D; Nolan G; Montine TJ; Galli SJ; West R; Bendall SC; Angelo M MIBI-TOF: A Multiplexed Imaging Platform Relates Cellular Phenotypes and Tissue Structure. Sci Adv 2019, 5, eaax5851. [PubMed: 31633026]

(22). Yagnik G; Liu Z; Rothschild K; Lim J, Highly MJ Multiplexed Immunohistochemical MALDI-MS Imaging of Biomarkers in Tissues. J Am Soc Mass Spectrom 2021, 32, 977–988. [PubMed: 33631930]

(23). Wehder L; Ernst G; Crecelius AC; Guntinas-Lichius O; Melle C; Schubert US; Von Eggeling F Depicting the Spatial Distribution of Proteins in Human Tumor Tissue Combining SELDI and MALDI Imaging and Immunohistochemistry. Journal of Histochemistry & Cytochemistry 2010, 58, 929–937. [PubMed: 20644210]

(24). Lundberg E; Borner GH Spatial Proteomics: A Powerful Discovery Tool for Cell Biology. Nat Rev Mol Cell Biol 2019, 20, 285–302. [PubMed: 30659282]

(25). Hattori T; Koide S Next-Generation Antibodies for Post-Translational Modifications. Curr Opin Struct Biol 2018, 51, 141–148. [PubMed: 29753204]

(26). Välikangas T; Suomi T; Elo LL A Comprehensive Evaluation of Popular Proteomics Software Workflows for Label-Free Proteome Quantification and Imputation. Brief Bioinform 2018, 19, 1344–1355. [PubMed: 28575146]

(27). Domon B; Aebersold R Options and Considerations When Selecting a Quantitative Proteomics Strategy. Nat Biotechnol 2010, 28, 710–721. [PubMed: 20622845]

(28). Zhu W; Smith JW; Huang CM Mass Spectrometry-Based Label-Free Quantitative Proteomics. J Biomed Biotechnol 2009, 2010, 840518. [PubMed: 19911078]

(29). Sobsey CA; Ibrahim S; Richard VR; Gaspar V; Mitsa G; Lacasse V; Zahedi RP; Batist G; Borchers CH Targeted and Untargeted Proteomics Approaches in Biomarker Development. Proteomics 2020, 20, 1900029.

(30). Palonpon AF; Sodeoka M; Fujita K Molecular Imaging of Live Cells by Raman Microscopy. Curr Opin Chem Biol 2013, 17, 708–715. [PubMed: 23773582]

(31). El-Mashtoly SF; Gerwert K Diagnostics and Therapy Assessment Using Label-Free Raman Imaging. Anal. Chem. 2021, 94, 120–142. [PubMed: 34852454]

(32). Rygula A; Majzner K; Marzec KM; Kaczor A; Pilarczyk M; Baranska M Raman Spectroscopy of Proteins: A Review. Journal of Raman Spectroscopy 2013, 44, 1061–1076.

(33). Hu F; Shi L; Min W Biological Imaging of Chemical Bonds by Stimulated Raman Scattering Microscopy. Nat Methods 2019, 16, 830–842. [PubMed: 31471618]

(34). Neumann EK; Djambazova KV; Caprioli RM; Spraggins JM Multimodal Imaging Mass Spectrometry: Next Generation Molecular Mapping in Biology and Medicine. J Am Soc Mass Spectrom 2020, 31, 2401–2415. [PubMed: 32886506]

(35). Diamandis EP Mass Spectrometry as a Diagnostic and a Cancer Biomarker Discovery Tool: Opportunities and Potential Limitations. Molecular and Cellular Proteomics 2004, 3, 367–378. [PubMed: 14990683]

(36). Soudah T; Zoabi A; Margulis K Desorption Electrospray Ionization Mass Spectrometry Imaging in Discovery and Development of Novel Therapies. Mass Spectrom Rev 2023, 42, 751–778. [PubMed: 34642958]

(37). Caprioli RM Imaging Mass Spectrometry: A Perspective. J Biomol Tech 2019, 30, 7–11. [PubMed: 30918475]

(38). Seeley EH; Caprioli RM Molecular Imaging of Proteins in Tissues by Mass Spectrometry. PNAS 2008, 105, 18126–18131. [PubMed: 18776051]

(39). Seeley EH; Caprioli RM MALDI Imaging Mass Spectrometry of Human Tissue: Method Challenges and Clinical Perspectives. Trends Biotechnol 2011, 29, 136–143. [PubMed: 21292337]

(40). Seeley EH; Caprioli RM 3D Imaging by Mass Spectrometry: A New Frontier. Anal. Chem. 2012, 84, 2105–2110. [PubMed: 22276611]

(41). Lemaire R; Desmons A; Tabet JC; Day R; Salzet M; Fournier I Direct Analysis and MALDI Imaging of Formalin-Fixed, Paraffin-Embedded Tissue Sections. J Proteome Res 2007, 6, 1295–1305. [PubMed: 17291023]

(42). Stauber J; Lemaire R; Franck J; Bonnel D; Croix D; Day R; Wisztorski M; Fournier I; Salzet M MALDI Imaging of Formalin-Fixed Paraffin-Embedded Tissues: Application to Model Animals of Parkinson Disease for Biomarker Hunting. J Proteome Res 2008, 7, 969–978. [PubMed: 18247558]

(43). Ryan DJ; Spraggins JM; Caprioli RM Protein Identification Strategies in MALDI Imaging Mass Spectrometry: A Brief Review. Curr Opin Chem Biol 2019, 48, 64–72. [PubMed: 30476689]

(44). Ryan DJ; Patterson NH; Putnam NE; Wilde AD; Weiss A; Perry WJ; Cassat JE; Skaar EP; Caprioli RM; Spraggins JM MicroLESA: Integrating Autofluorescence Microscopy, in Situ Micro-Digestions, and Liquid Extraction Surface Analysis for High Spatial Resolution Targeted Proteomic Studies. Anal Chem 2019, 91, 7578–7585. [PubMed: 31149808]

(45). Stauber J; MacAleese L; Franck J; Claude E; Snel M; Kaletas BK; Wiel IM; Wisztorski M; Fournier I; Heeren RM On-Tissue Protein Identification and Imaging by MALDI-Ion Mobility Mass Spectrometry. J Am Soc Mass Spectrom 2010, 21, 338–347. [PubMed: 19926301]

(46). Delcourt V; Franck J; Quanico J; Gimeno JP; Wisztorski M; Raffo-Romero A; Kobeissy F; Roucou X; Salzet M; Fournier I Spatially-Resolved Top-down Proteomics Bridged to MALDI MS Imaging Reveals the Molecular Physiome of Brain Regions. Molecular and Cellular Proteomics 2018, 17, 357–372. [PubMed: 29122912]

(47). Zavalin A; Yang J; Hayden K; Vestal M; Caprioli RM Tissue Protein Imaging at 1 μm Laser Spot Diameter for High Spatial Resolution and High Imaging Speed Using Transmission Geometry MALDI TOF MS. Anal. Bioanal. Chem. 2015, 407, 2337–2342. [PubMed: 25673247]

(48). Zhu Y; Piehowski PD; Zhao R; Chen J; Shen Y; Moore RJ; Shukla AK; Petyuk VA; Campbell-Thompson M; Mathews CE; Smith RD; Qian WJ; Kelly RT Nanodroplet Processing Platform for Deep and Quantitative Proteome Profiling of 10–100 Mammalian Cells. Nat Commun 2018, 9, 882. [PubMed: 29491378]

(49). Piehowski PD; Zhu Y; Bramer LM; Stratton KG; Zhao R; Orton DJ; Moore RJ; Yuan J; Mitchell HD; Gao Y; Webb-Robertson BJM; Dey SK; Kelly RT; Burnum-Johnson KE Automated Mass Spectrometry Imaging of over 2000 Proteins from Tissue Sections at 100-Mm Spatial Resolution. Nat Commun 2020, 11, 8. [PubMed: 31911630]

(50). Siuti N; Kelleher NL Decoding Protein Modifications Using Top-down Mass Spectrometry. Nat Methods 2007, 4, 817–821. [PubMed: 17901871]

(51). Smith LM; Kelleher NL Proteoform: A Single Term Describing Protein Complexity. Nat Methods 2013, 10, 186–187. [PubMed: 23443629]

(52). Aebersold R; Agar JN; Amster IJ; Baker MS; Bertozzi CR; Boja ES; Costello CE; Cravatt BF; Fenselau C; Garcia BA; Ge Y; Gunawardena J; Hendrickson RC; Hergenrother PJ; Huber CG; Ivanov AR; Jensen ON; Jewett MC; Kelleher NL; Kiessling LL; Krogan NJ; Larsen MR; Loo JA; Ogorzalek Loo RR; Lundberg E; Maccoss MJ; Mallick P; Mootha VK; Mrksich M; Muir TW; Patrie SM; Pesavento JJ; Pitteri SJ; Rodriguez H; Saghatelian A; Sandoval W; Schlüter H; Sechi S; Slavoff SA; Smith LM; Snyder MP; Thomas PM; Uhlén M; Van Eyk JE; Vidal M; Walt DR;

White FM; Williams ER; Wohlschlager T; Wysocki VH; Yates NA; Young NL; Zhang B How Many Human Proteoforms Are There? Nat Chem Biol 2018, 14, 206–214. [PubMed: 29443976]

(53). Parekh RB; Rohlff C Post-Translational Modification of Proteins and the Discovery of New Medicine. Curr Opin Biotechnol 1997, 8, 718–723. [PubMed: 9425663]

(54). Smith LM; Agar JN; Chamot-Rooke J; Danis PO; Ge Y; Loo JA; Paša-Tolić L; Tsybin YO; Kelleher NL; Consortium for Top-Down Proteomics. The Human Proteoform Project: Defining the Human Proteome. Sci Adv 2021, 7, eabk0734. [PubMed: 34767442]

(55). Griffiths RL; Kocurek KI; Cooper HJ Ambient Surface Mass Spectrometry – Ion Mobility Spectrometry of Intact Proteins. Curr Opin Chem Biol 2018, 42, 67–75. [PubMed: 29166625]

(56). Towers MW; Karancsi T; Jones EA; Pringle SD; Claude E Optimised Desorption Electrospray Ionisation Mass Spectrometry Imaging (DESI-MSI) for the Analysis of Proteins/Peptides Directly from Tissue Sections on a Travelling Wave Ion Mobility Q-ToF. J. Am. Soc. Mass Spectrom. 2018, 29, 2456–2466. [PubMed: 30168053]

(57). Garza KY; Feider CL; Klein DR; Rosenberg JA; Brodbelt JS; Eberlin LS Desorption Electrospray Ionization Mass Spectrometry Imaging of Proteins Directly from Biological Tissue Sections. Anal Chem 2018, 90, 7785–7789. [PubMed: 29800516]

(58). Hale OJ; Cooper HJ Native Mass Spectrometry Imaging and in Situ Top-Down Identification of Intact Proteins Directly from Tissue. J Am Soc Mass Spectrom 2020, 31, 2531–2537. [PubMed: 32822168]

(59). Hale OJ; Sisley EK; Griffiths RL; Styles IB; Cooper HJ Native LESA TWIMS-MSI: Spatial, Conformational, and Mass Analysis of Proteins and Protein Complexes. J Am Soc Mass Spectrom 2020, 31, 873–879. [PubMed: 32159346]

(60). Yang M; Hu H; Su P; Thomas PM; Camarillo JM; Greer JB; Early BP; Fellers RT; Kelleher NL; Laskin J Proteoform-Selective Imaging of Tissues Using Mass Spectrometry. Angew. Chem. Int. Ed. 2022, 61, e202200721.

(61). Su P; Mcgee JP; Durbin KR; Hollas MAR; Yang M; Neumann EK; Allen JL; Drown BS; Butun FA; Greer JB; Early BP; Fellers RT; Spraggins JM; Laskin J; Camarillo JM; Kafader JO; Kelleher NL Highly Multiplexed, Label-Free Proteoform Imaging of Tissues by Individual Ion Mass Spectrometry. Sci Adv 2022, 8, eabp9929. [PubMed: 35947651]

(62). J. Hale O.; J. Cooper H. Native Mass Spectrometry Imaging of Proteins and Protein Complexes by Nano-DESI. Anal Chem 2021, 93, 4619–4627. [PubMed: 33661614]

(63). Hale OJ; Hughes JW; Sisley EK; Cooper HJ Native Ambient Mass Spectrometry Enables Analysis of Intact Endogenous Protein Assemblies up to 145 kDa Directly from Tissue. Anal Chem 2022, 94, 5608–5614. [PubMed: 35358391]

(64). Sisley EK; Hale OJ; Styles IB; Cooper HJ Native Ambient Mass Spectrometry Imaging of Ligand-Bound and Metal-Bound Proteins in Rat Brain. J. Am. Chem. Soc 2022, 144, 2120–2128. [PubMed: 35077646]

(65). Hsu CC; Chou PT; Zare RN Imaging of Proteins in Tissue Samples Using Nanospray Desorption Electrospray Ionization Mass Spectrometry. Anal Chem 2015, 87, 11171–11175. [PubMed: 26509582]

(66). Yin R; Burnum-Johnson KE; Sun X; Dey SK; Laskin J High Spatial Resolution Imaging of Biological Tissues Using Nanospray Desorption Electrospray Ionization Mass Spectrometry. Nat Protoc 2019, 14, 3445–3470. [PubMed: 31723300]

(67). Unsihuay D; Yin R; Mesa D; Yang M; Li Y; Sun X; Dey SK; Laskin J High-Resolution Imaging and Identification of Biomolecules Using Nano-DESI Coupled to Ion Mobility Spectrometry. Anal Chim Acta 2021, 1186, 339085. [PubMed: 34756271]

(68). Unsihuay D; Su P; Hu H; Qiu J; Kuang S; Li Y; Sun X; Dey SK; Laskin J Imaging and Analysis of Isomeric Unsaturated Lipids through Online Photochemical Derivatization of Carbon–Carbon Double Bonds. Angew. Chem. Int. Ed. 2021, 60, 7559–7563.

(69). Jaszczyk A; Stankiewicz AM; Juszczak GR Dissection of Mouse Hippocampus with Its Dorsal, Intermediate and Ventral Subdivisions Combined with Molecular Validation. Brain Sci 2022, 12, 799. [PubMed: 35741684]

(70). Jackson-Lewis V; Przedborski S Protocol for the MPTP Mouse Model of Parkinson's Disease. Nat Protoc 2007, 2, 141–151. [PubMed: 17401348]

(71). Seeley EH; Oppenheimer SR; Mi D; Chaurand P; Caprioli RM Enhancement of Protein Sensitivity for MALDI Imaging Mass Spectrometry After Chemical Treatment of Tissue Sections. J Am Soc Mass Spectrom 2008, 19, 1069–1077. [PubMed: 18472274]

(72). Schaffer LV; Millikin RJ.; Miller RM.; Anderson LC.; Fellers RT.; Ge Y.; Kelleher NL.; Leduc RD.; Liu X.; Payne SH.; Sun L.; Thomas PM.; Tucholski T.; Wang Z.; Wu S.; Wu Z.; Yu D.; Shortreed MR.; Smith LM. Identification and Quantification of Proteoforms by Mass Spectrometry. Proteomics 2019, 19, 1800361.

(73). Apweiler R; Bairoch A; Wu CH; Barker WC; Boeckmann B; Ferro S; Gasteiger E; Huang H; Lopez R; Magrane M; Martin MJ; Natale DA; O'donovan C; Redaschi N; Yeh LSL UniProt: The Universal Protein Knowledgebase. Nucleic Acids Res 2004, 32, D115–D119. [PubMed: 14681372]

(74). The UniProt Consortium. UniProt: A Hub for Protein Information. Nucleic Acids Res 2015, 43, D204–D212. [PubMed: 25348405]

(75). The UniProt Consortium. UniProt: A Worldwide Hub of Protein Knowledge. Nucleic Acids Res 2019, 47, D506–D515. [PubMed: 30395287]

(76). Mesa Sanchez D; Creger S; Singla V; Kurulugama RT; Fjeldsted J; Laskin J Ion Mobility-Mass Spectrometry Imaging Workflow. J Am Soc Mass Spectrom 2020, 31, 2437–2442. [PubMed: 32841564]

(77). Barbarese E; Barry C; Chou CHJ; Goldstein DJ; Nakos GA; Hyde-DeRuyscher R; Scheld K; Carson JH Expression and Localization of Myelin Basic Protein in Oligodendrocytes and Transfected Fibroblasts. J Neurochem 1988, 51, 1737–1745. [PubMed: 2460587]

(78). Bradl M; Lassmann H Oligodendrocytes: Biology and Pathology. Acta Neuropathol 2010, 119, 37–53. [PubMed: 19847447]

(79). Duncan KD; Lanekoff I Oversampling to Improve Spatial Resolution for Liquid Extraction Mass Spectrometry Imaging. Anal Chem 2018, 90, 2451–2455. [PubMed: 29373011]

(80). Li X; Hu H; Yin R; Li Y; Sun X; Dey SK; Laskin J High-Throughput Nano-DESI Mass Spectrometry Imaging of Biological Tissues Using an Integrated Microfluidic Probe. Anal Chem 2022, 94, 9690–9696. [PubMed: 35770488]

(81). Colliver TL; Brummel CL; Pacholski ML; Swanek FD; Ewing AG; Winograd N Atomic and Molecular Imaging at the Single-Cell Level with TOF-SIMS. Anal Chem 1997, 69, 2225–2231. [PubMed: 9212701]

(82). Laskin J; Heath BS; Roach PJ; Cazares L; Semmes OJ Tissue Imaging Using Nanospray Desorption Electrospray Ionization Mass Spectrometry. Anal. Chem 2012, 84, 141–148. [PubMed: 22098105]

(83). Metodiev MD; Steven RT; Loizeau X; Takats Z; Bunch J Modality Agnostic Model for Spatial Resolution in Mass Spectrometry Imaging: Application to MALDI MSI Data. Anal Chem 2021, 93, 15295–15305. [PubMed: 34767361]

(84). Eberlin LS; Liu X; Ferreira CR; Santagata S; Agar NY; Cooks RG Desorption Electrospray Ionization Then MALDI Mass Spectrometry Imaging of Lipid and Protein Distributions in Single Tissue Sections. Anal Chem 2011, 83, 8366–8371. [PubMed: 21975048]

(85). Kaya I; Brinet D; Michno W; Başkurt M; Zetterberg H; Blenow K; Hanrieder J Novel Trimodal MALDI Imaging Mass Spectrometry (IMS3) at 10 μm Reveals Spatial Lipid and Peptide Correlates Implicated in Aβ Plaque Pathology in Alzheimer's Disease. ACS Chem Neurosci 2017, 8, 2778–2790. [PubMed: 28925253]

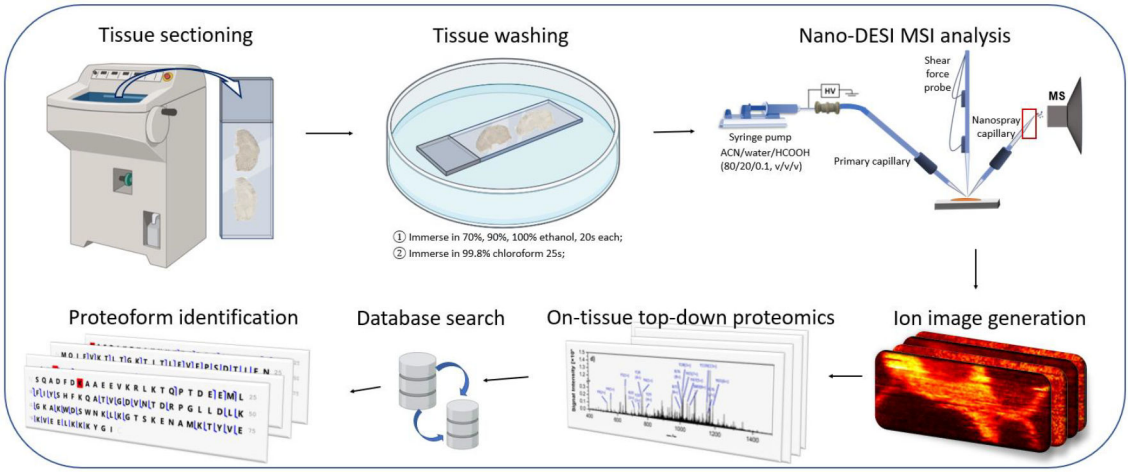

Figure 1.

The experimental workflow for nano-DESI MSI of proteins in tissue sections. The individual steps are described in detail in the experimental section.

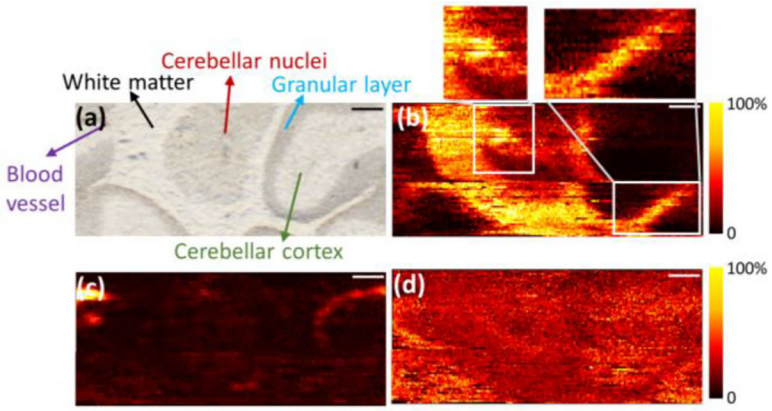

Figure 2.

High-resolution imaging of proteins in the cerebellum region of a sagittal mouse brain tissue section acquired using a 15 μm step between the lines. (a) An optical image of the tissue section. Ion images of proteoforms normalized to TIC: (b) m/z 614.966^{23+}, 14,121 Da, myelin basic protein, N-terminal acetylation, zoomed-in images of the regions labeled with white square are shown above; (c) m/z 882.221^{17+}, 14,981 Da, hemoglobin subunit alpha, modification unknown; (d) m/z 779.612^{11+}, 8,565 Da, ubiquitin, unmodified. Scale bar: 250 μm.

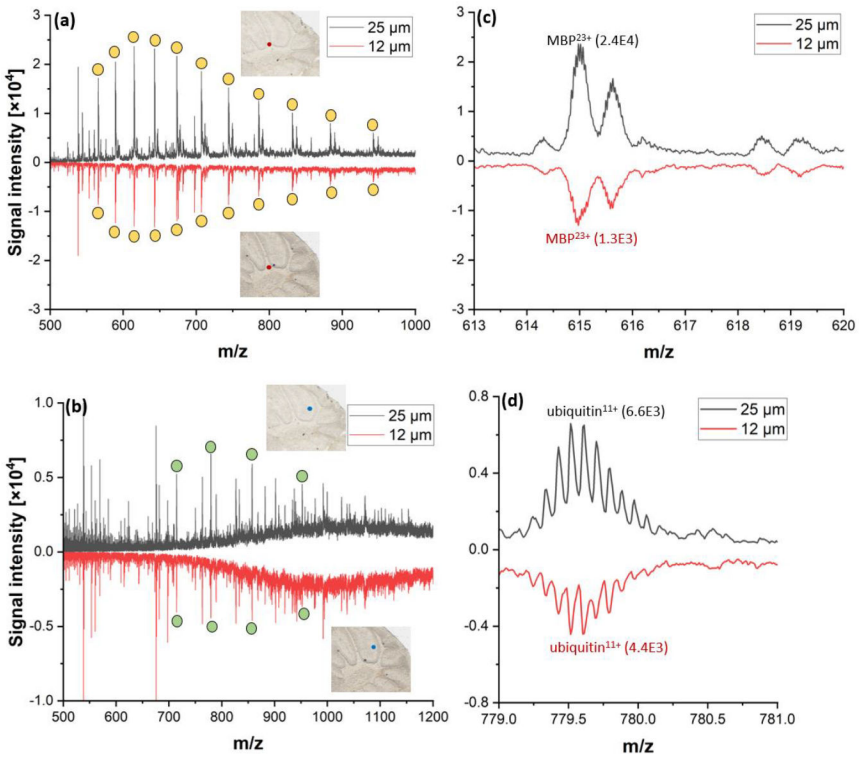

Figure 3.

Mass spectra averaged over 6 pixels of the circled region in the optical images, showing protein signals in the (a) white matter region and (b) cerebellar cortex region of a 25 µm-thick (black) and 12 µm-thick (red) tissue section. Different charge states of the most abundant protein in (a, b) are labeled with orange dots (MBP) and green dots (ubiquitin). Zoomed-in mass spectra from (a, b) show the signals of the most abundant charge states of the (c) 14.1 kDa MBP, MBP^{23+} and (d) 8.5 kDa ubiquitin, $ubquitin^{11+}$ with the signal intensity of the most abundant isotopic peak labeled in the panels.

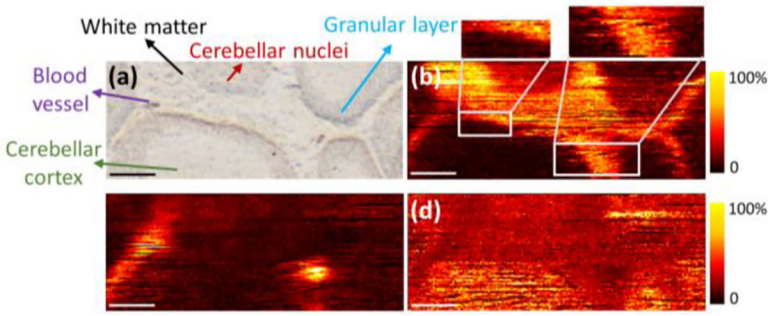

Figure 4.

7 μm step: (a) An optical image of a sagittal mouse brain tissue section. Ion images of the proteoforms normalized to TIC: (b) m/z 614.910^{23+}, 14,120 Da, myelin basic protein, N-terminal acetylation, zoomed-in images of the regions labeled with white square are shown above; (c) m/z 882.125^{17+}, 14,979 Da, hemoglobin subunit alpha, modification unknown; (d) m/z 779.539^{11+}, 8,564 Da, ubiquitin, unmodified. Scale bar: 250 μm.

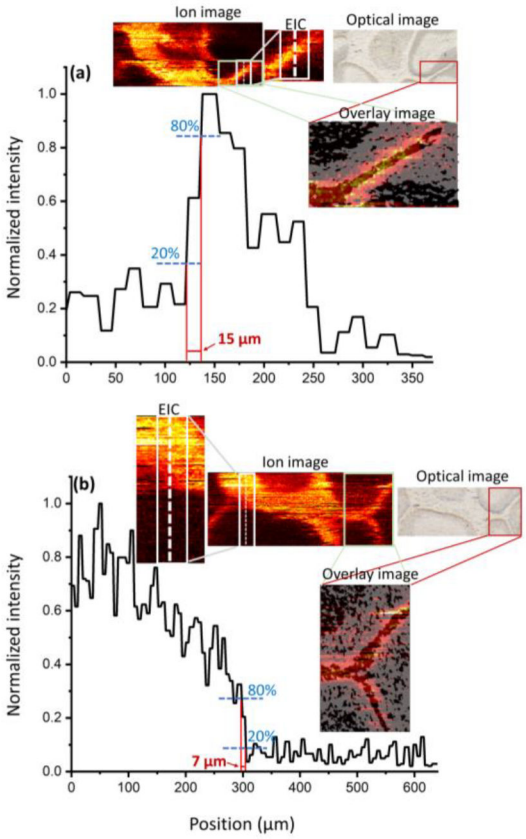

Figure 5.

Extracted ion chronograms (EIC) along the white line for spatial resolution calculations: (a) 15 µm step, (b) 7 µm step. Signals are normalized to the maximum signal of a selected *m/z* along the line. An overlay of the optical image and the ion image of MBP^{23+} in a small region of interest for both datasets are shown besides each figure.

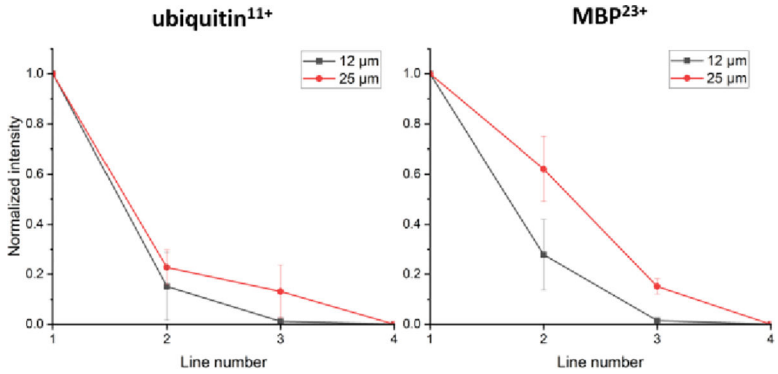

Figure 6.

Depletion curves for the four repeated line scans on (a) cerebellar cortex region for the most abundant isotopic peak of 11+ charge state ubiquitin, and (b) white matter region for the most abundant isotopic peak of 23+ charge state MBP of 25 μm (black) and 12 μm (red) tissue sections (N=3). The background signal was obtained from the fourth scan and subtracted from the signals observed in the first three scans; background subtraction was followed by normalization to the highest intensity.